Applied Magnetic Resonance (2018) 49:1299–1311
https://doi.org/10.1007/s00723-018-1053-7

Applied
Magnetic Resonance

ORIGINAL PAPER

Cu(II) EPR Reveals Two Distinct Binding Sites and Oligomerization of Innate Immune Protein Calgranulin C

Shreya Ghosh, et al. ***[full author details at the end of the article]***

Received: 21 June 2018 / Revised: 23 July 2018 / Published online: 17 August 2018

Abstract

S100A12 or Calgranulin C is a homodimeric antimicrobial protein of the S100 family of EF-hand calcium-modulated proteins. S100A12 is involved in many diseases such as inflammation, tumor invasion, cancer and neurological disorders such as Alzheimer's disease. The binding of transition metal ions to the protein is important as the sequestering of the metal ion induces conformational changes in the protein, inhibiting the growth of various pathogenic microorganisms. In this work, we probe the Cu^{2+} binding properties of Calgranulin C. We demonstrate that the two Cu^{2+} binding sites in Calgranulin C show different coordination environments in solution. Continuous wave-electron spin resonance (CW-ESR) spectra of Cu^{2+}-bound protein clearly show two distinct components at higher Cu^{2+}:protein ratios, which is indicative of the two different binding environments for the Cu^{2+} ions. The $g_{\|}$ and $A_{\|}$ values are also different for the two components, indicating that the number of directly coordinated nitrogen in each site differs. Furthermore, we perform CW-ESR titrations to obtain the binding affinity of the Ca^{2+}-loaded protein to Cu^{2+} ions. We observe a positive cooperativity in binding of the two Cu^{2+} ions. To further probe the Cu^{2+} coordination, we also perform electron spin echo envelope modulation (ESEEM) experiment. We perform ESEEM at two different fields where one Cu^{2+} binding site dominates the other. At both sites we see distinct signatures of Cu^{2+}–histidine coordination. However, we clearly see that the ESEEM spectra corresponding to the two Cu^{2+} binding sites are significantly different. There is clear change in the intensity of the double quantum peak with respect to the nuclear quadrupole interaction peak at the two different fields. Furthermore, ESEEM along with hyperfine sublevel correlation show that only one of the two Cu^{2+} binding sites has backbone coordination, confirming our previous observation. Finally, we perform double electron–electron resonance spectroscopy to probe if the difference in binding environment is due to the Cu^{2+} binding to different sites in the protein. We obtain a distance distribution with a sharp peak at ~3 nm and a broad peak at ~4 nm. The shorter distance agrees with the Cu^{2+}–Cu^{2+} distance expected for a dimer from the crystal structure. The longer distance is consistent with the Cu^{2+}–Cu^{2+} distance when oligomerization occurs.

1 Introduction

Calgranulin C or S100A12 is a member of the S100 class of EF-hand calcium (Ca^{2+})-binding proteins. There are ~ 20 S100 proteins which are expressed in a tissue and cell-specific manner and act intracellularly to regulate a diverse array of biological functions including Ca^{2+} homeostasis, cell proliferation, and energy metabolism [1]. Additionally, a number of S100 proteins are exported from cells where they activate signaling mechanisms and act as antimicrobial agents [2, 3]. The biological relevance of S100 proteins is underscored by the misregulation of their expression in a number of diseases such as Alzheimer's disease, diabetes, cancer and inflammatory disorders [4–6].

In addition to binding calcium, several S100 proteins bind divalent transition metals, most notably Zn^{2+}. S100A7 and S100A15 bind zinc, and the S100A8/S100A9 heterodimer calprotectin binds zinc and manganese as part of the host innate immune response to starve pathogens, a mechanism termed nutritional immunity [7–11]. S100A12 zinc sequestration has been implicated in the control of *H. pylori* and *Campylobacter jejuni* infections [12, 13]. Additionally, Zn^{2+} binding to S100A12 and S100A7 has been implicated in activation of the receptor for advanced glycation end products, an inflammation receptor [14, 15].

Compared to Zn^{2+}, less is known about the role of Cu^{2+} in the function of S100 proteins. Copper is an important metal in the innate immune response. Copper is accumulated at sites of infection in the phagosomes of macrophages and can produce reactive oxygen species [16, 17]. The general mechanism of Cu^{2+} is based on its toxicity to bacterial pathogens [18]. However, recently it was shown that calprotectin starves Cu^{2+} and Zn^{2+} as part of the innate immune response toward *Candida albicans* [19]. Several S100 proteins bind copper, including S100B, S100A13, S100A5, Calprotectin, and S100A12 [19–24]. Whether copper sequestration by S100 proteins is a general innate immune mechanism remains to be determined. Given the similarity between Zn^{2+} and Cu^{2+}, the possibility that Cu^{2+} potentiates activation of inflammatory receptors is also feasible.

S100A12 adopts the classic S100 protein fold, as shown in Fig. 1. Two subunits of 92 amino acids, each comprised of two helix–loop–helix EF-hand motifs separated by a hinge region, are arranged in an antiparallel homodimer. Similar to the related proteins S100B, S100A7, S100A8, and S100A9, there are two transition metal binding sites located at opposite ends of the dimer interface. Each metal binding site is believed to comprise two histidines from one subunit and a histidine and aspartic (or glutamic) acid in the other. These canonical transition metal binding sites are highly conserved in S100 proteins. In S100A12, each metal binding site is comprised of His-15 and Asp-25 of one subunit and His-85 and His-89 from the other, as shown in Fig. 1. The X-ray crystal structure of Ca^{2+}–Cu^{2+}–S100A12 has been determined to be 2.19 Å resolution [20]. In comparison to the Ca^{2+}–S100A12 structure, there is little change to the overall tertiary structure upon copper binding. The most significant conformational change is the elongation of the C-terminal helix of Cu^{2+}–Ca^{2+}–S100A12 by four residues which include the Cu^{2+}-chelating residue His89. In stark contrast, the quaternary

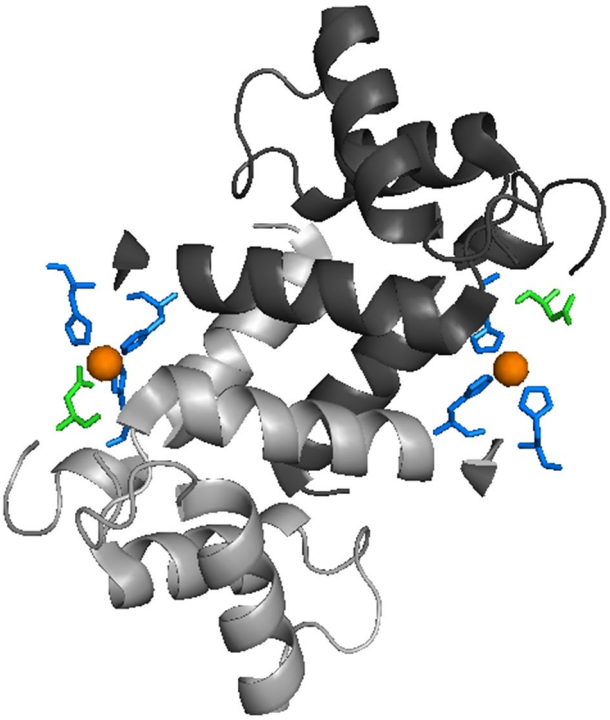

Fig. 1 Dimer of S100A12 (PDB: 1ODB). The two subunits are shown in dark and light gray. The blue sticks denote the histidine residues while the green denotes aspartic acid. The orange spheres represent the Cu^{2+} ions. So far crystal structure (PDB: 1ODB) [20] predicts that in an S100A12 dimer, each metal binding site is comprised of His-15 and Asp-25 of one subunit and His-85 and His-89 from the other. However, in solution, we see distinct differences between the binding environments of the two Cu^{2+} binding sites (color figure online)

structure of Cu^{2+}–Ca^{2+}–S100A12 is drastically different from apo-S100A12. Similar to Zn^{2+} and Ca^{2+} complexes of S100A12 which form dimers, tetramers, and hexamers [25–27], Cu^{2+} induces oligomerization of Ca^{2+}–S100A12 into a trimer of dimers. It has been proposed that oligomeric forms of S100A12 are required for its activation of the RAGE inflammation receptor [27, 28]. However, to date, no link between Cu^{2+} and S100A12-RAGE signaling has been established.

Despite the importance of Cu^{2+}, relatively few studies have focused on the interaction of Cu^{2+} with S100A12 in solution. Here, we describe electron spin resonance (ESR) studies to characterize the Cu^{2+} binding site of Ca^{2+}–S100A12, and the effect of Cu^{2+} on S100A12 oligomerization. First, we use continuous wave (CW)-ESR to show that there are two distinct binding sites. This interpretation is supported by pulsed electron spin echo envelope modulation (ESEEM) experiments that show differences in the spectra between the two sites, with backbone coordination to Cu^{2+} shown at only one of the sites. Hyperfine sublevel correlation (HYSCORE) experiments also validate the presence of backbone coordination for only one of the Cu^{2+} binding sites. Finally, we explore the

structure and oligomerization using double electron–electron resonance (DEER) measurements.

2 Materials and Methods

2.1 Sample Preparation

The expression and purification of S100A12 were performed as previously described [29]. $CaCl_2$ solution, prepared in MQ H_2O, was added to the protein in a 4:1 ratio. $CuCl_2$ solution, prepared in water, was added to the calcium-bound protein as necessary.

2.2 ESR Measurements

The samples were prepared in 50 mM *N*-ethylmorpholine (NEM) buffer, pH 7.4, to eliminate any free Cu^{2+} signal [30]. Glycerol (20% v/v) was added as a cryoprotectant. All sample volumes were 120 µL. ESR experiments were performed on either a Bruker ElexSys E680 X-band FT/CW spectrometer equipped with a Bruker EN4118X-MD4 resonator or a Bruker ElexSys 580 X-band FT/CW spectrometer equipped with a Bruker ER4118X-MD5 resonator. The temperature for all experiments was controlled using an Oxford ITC503 temperature controller with an Oxford ER 4118CF gas flow cryostat.

Continuous wave (CW)-ESR experiments were carried out at X-band frequencies at 80 K. Data were collected for 1024 points over a sweep width of 2000 G, from 2100 G to 4100 G, with a modulation amplitude of 4 G. The CW-ESR data were acquired with a modulation frequency of 100 kHz, a time constant of 10.24 ms, a conversion time of 20.48 ms and an incident power of 0.1992 mw. All CW spectra were simulated and fit using the EasySpin software [31].

Three-pulse electron spin envelope echo modulation (ESEEM) experiments were performed at X-band frequencies at 80 K. A $\pi/2-\tau-\pi/2-T-\pi/2$–echo pulse sequence with a $\pi/2$ pulse length of 16 ns was used. The first time delay, τ, was set to 144 ns for ESEEM performed at 2807 G and 152 ns for 3430 G. The second time delay, T, was varied, starting from an initial value of 288 ns with a step size of 16 ns. A four-step phase cycling was employed to eliminate all unwanted echoes [32, 33]. Data acquisition took ~ 12 h. The resultant signal was phase corrected, baseline subtracted and Fourier-transformed using the Bruker WinEPR software.

Four-pulse hyperfine sublevel correlation (HYSCORE) experiments were performed at 20 K at X-band frequencies. The pulse sequence $\pi/2-\tau-\pi/2-t_1-\pi-t_2-\pi/2-\tau$–echo was used. HYSCORE was performed at two fields. At 2807 G, the first pulse separation, τ was set at 144 ns while at 3430 G, τ was set at 152 ns. The pulse separations, t_1 and t_2, were varied from 200 ns with a step size of 16 ns for a total of 256 points. The pulse lengths used were 16 ns and 32 ns for $\pi/2$ and π pulses, respectively. A four-step phase cycling eliminated unwanted echo. The real parts of the collected two-dimensional data were phase corrected,

baseline subtracted and zero filled to 512 points in both dimensions using the Bruker WinEPR software. The data were then fast Fourier transformed and reported as a contour plot.

Double electron–electron resonance (DEER) experiments were performed at 20 K at X-band frequencies. The four-pulse sequence used was $(\pi/2)\nu_1$–τ_1–$(\pi)\nu_1$–(τ_1+t)–$(\pi)\nu_2$–$(\tau_1+\tau_2-t)$–$(\pi)\nu_1$–τ_2–echo [34]. The observer pulses, $(\pi/2)\nu_1$ and $(\pi)\nu_1$ were 16 ns and 32 ns, respectively, and the pump pulse $(\pi)\nu_2$ was 16 ns. The delay, t, was incremented using a step size of 14 ns for a total of 128 points. The pump frequency, ν_2, was placed at the maximum of the echo-detected field swept spectrum with the observer frequency, ν_1, offset 150 MHz downfield. The raw time domain DEER data were analyzed by DEERAnalysis2015b [35] via Tikhonov regularization. Distance distribution was corrected using proper g values [36]. Data acquisition took ~ 24 h.

3 Results and Discussion

We first performed CW-ESR titrations to obtain the maximum loading efficiency of the Cu^{2+} to the Ca^{2+}-bound S100A12 protein and consequently, the binding affinity of Cu^{2+} to the native Cu^{2+}-binding sites in the protein. Figure 2a shows the CW-ESR spectra of the protein at different Cu^{2+} equivalents. Figure 2b shows the CW spectrum of 1 Cu^{2+} equivalent along with the best fit. The simulation indicates a single component fit with $g_{\|}$ and $A_{\|}$ values of 2.335 and 118 G, respectively. We refer to this binding environment as component 1. Around 3 Cu^{2+} equivalents, the CW spectrum showed a distinct second component (cf. Fig. 2c), which is easily distinguishable in the $g_{\perp}$ region. Simulations of the spectrum at 3.5 Cu^{2+} equivalents confirmed the presence of two components. The second component corresponded to $g_{\|}$ and $A_{\|}$ values of 2.292 and 115 G, respectively. The difference in $g_{\|}$ (2.335 and 2.292) between the first and the second components indicates differences in the coordination environment of copper. The $A_{\|}$ values of the two components indicate that the copper in S100A12 is a type II copper center which forms tetrahedral

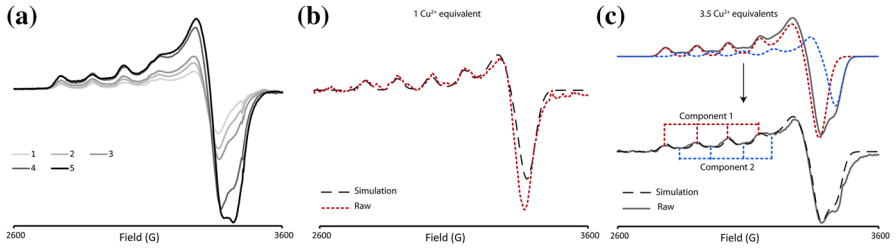

Fig. 2 **a** CW-ESR titrations performed at different Cu^{2+} equivalents. **b** Simulations show that the CW-ESR spectrum at 1 equivalent of Cu^{2+} is a single component with $g_{\|}$ and $A_{\|}$ values of 2.335 and 118 G, respectively. **c** At 3.5 equivalents of Cu^{2+}, a distinct second component is observed. Hence, we use another component with $g_{\|}$ and $A_{\|}$ of 2.292 and 115 G (blue dotted lines, upper panel). By varying the ratios of the two components we get the best fit for the spectrum, as shown in the lower panel (color figure online)

geometry, which is consistent with the Ca^{2+}–Cu^{2+} crystal structure of S100A12 [20] and previously reported data from ESR studies on the Cu^{2+}–S100A12 (without Ca^{2+}) [37].

The CW-ESR results are interesting when compared to the crystal structure of Ca^{2+}–S100A12 crystallized in the presence of excess Cu^{2+} (PDB 1ODB) [20]. Three homodimers of S100A12 arranged as a hexamer are present in the asymmetric unit which results in six total Cu^{2+} ions in the structure. Five of the Cu^{2+} binding sites are canonical S100 transition metal binding sites comprised of a histidine and aspartic acid (His15 and Asp25) from one subunit of the dimer and two histidine residues from the other subunit (His85 and His 89). However, in one of the dimers, the canonical Cu^{2+} binding site is altered. Asp25 is replaced by Glu55 from a symmetry-related molecule. This results in a larger Cu–O distance as compared to the Asp–Cu^{2+} coordination in the other sites (2.4 vs 2.05) [14]. This non-canonical coordination may be an artifact from crystal packing. However, a study of Zn^{2+} binding to Ca^{2+}–S100B revealed that different ligands coordinate Zn^{2+} at different pH, which suggest the residues in the transition metal binding sites of S100 proteins may be dynamic [38]. Other studies have shown the canonical transition metal binding site may be modified by external ligands. For example, S100A15 has the required aspartic acid residue replaced with a glycine. A chloride ion serves as the fourth zinc ligand in the Zn^{2+}–S100A15 crystal structure [39]. Additionally, the Zn^{2+}–Ca^{2+}–S100A8 homodimer structure has His27 replaced with a chloride ion in two out of the eight molecules in the asymmetric unit [40]. In total, these data suggest that the transition metal binding sites in S100 proteins may be more flexible than previously thought. Hence, it is possible to observe slight differences in the predicted equivalent Cu^{2+} binding sites of S100A12. From the $A_{\|}$ and $g_{\|}$ values that we report, Cu^{2+} shows difference in its binding environment. This suggests that in solution the two symmetrical Cu^{2+} binding sites in S100A12 behave differently. Indeed, literature reports that even though proteins of S100 family are known to be typically homodimers, they can adopt overall asymmetric conformations upon metal binding [7].

Next, we established the mode of binding of Cu^{2+} to Ca^{2+}-bound S100A12 in solution. The double integrated intensity of the CW-ESR spectrum is related to the concentration of the bound Cu^{2+}. Note that the data were acquired in NEM buffer where free Cu^{2+} is ESR silent [30, 41]. By comparing to a standard, the concentration of bound Cu^{2+} can be determined [42–45]. Figure 3 shows the ratio of bound Cu^{2+}:protein as a function of total equivalents of added Cu^{2+}. We fit these data to different binding models. The first model we considered was independent binding to the two sites [43]. The fit is shown by a dotted line in Fig. 3. The second model we tried was the Klotz equation [46, 47] (Fig. 3, dashed line). The Klotz model considers cooperative binding between the two binding sites with different binding affinities for each site. Lastly, we applied the Hill's equation [48–50] to fit our data (Fig. 3, solid line). As can be seen, our data best fit the binding affinity model described by Hill's equation. The apparent dissociation constant K_d can be then calculated from the Hill's equation as

$$\theta = \frac{[L]^n}{K_d + [L]^n},$$

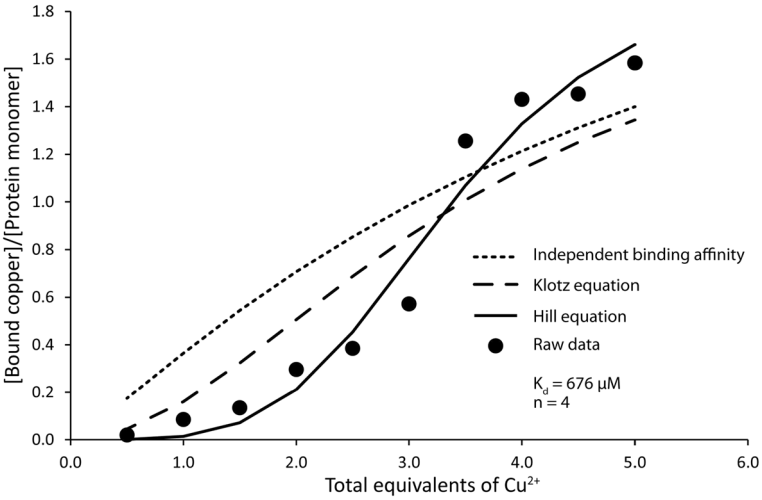

Fig. 3 Plot showing the bound Cu^{2+} concentration/protein monomer concentration versus total equivalents of Cu^{2+}. Protein monomer concentration is 200 µM. The raw data were fitted to three different models. The model corresponding to the Hill equation best fits the data. The apparent dissociation constant using the Hill equation was found to be 676 µM with a positive cooperativity of 4

where θ is the fraction of protein bound to ligand, [L] is the concentration of the free (unbound) ligand, K_d is the apparent dissociation constant and n is the Hill's coefficient. A value of n greater than 1 is associated with positive cooperative binding. For our data, the Hill's coefficient of 4 indicates that the binding of a ligand molecule at one site facilitates the binding of the same ligand at a different site. Thus, affinity of the second site towards the ligand increases and results in positive cooperative binding. The apparent K_d value of Cu^{2+} bound to Ca^{2+}–S100A12 is 676 µM. This apparent K_d likely reflects a complex process involving binding of Cu^{2+} to Ca^{2+}–S100A12 and oligomerization of Cu^{2+}–Ca^{2+}–S100A12 (see below). Factors such as temperature, buffer, and pH largely affect the apparent K_d. Most importantly, our measured value is at 80 K and the affinity at physiological conditions is expected to be much higher [44].

To confirm our findings, we performed ESEEM experiments at two different fields (Fig. 4b, inset, red lines) on the S100A12 with 3.5 equivalents of Cu^{2+} (Fig. 4). Analysis of the CW-ESR simulations indicated that at a field of 2807 G, the spectrum consists of 98% of the first component while at 3430 G, the second component constitutes ~ 92% of the spectrum (Fig. 4a, b inset). Therefore, ESEEM experiments were performed at these two fields to probe Cu^{2+} coordination at each site. These positions are shown in red in the inset of Fig. 4b. ESEEM is mainly sensitive to weak hyperfine interactions, which normally are not resolved in the broad CW-ESR spectra. For Cu^{2+} bound to histidines a characteristic ESEEM spectrum is observed [51, 52]. Nuclear quadrupole interactions (NQI) of ^{14}N give rise to three sharp peaks below 2 MHz in the ESEEM spectra. A broad feature around 4 MHz is due to the double quantum (DQ) transition of the remote nitrogen in an imidazole ring. The ESEEM spectra also show significant changes with changes in the number

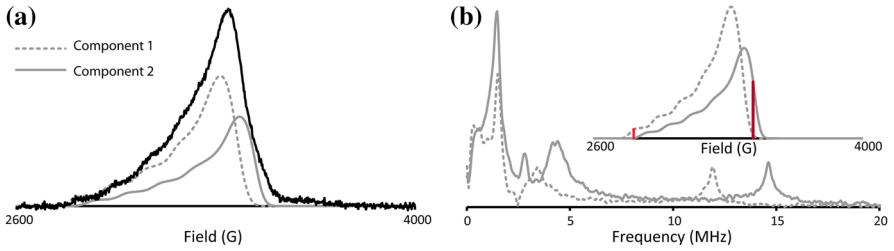

Fig. 4 **a** Echo-detected field swept spectrum of S100A12 with 3.5 Cu^{2+} equivalents (black solid). The simulated spectra corresponding to the first component (gray dotted) and second component (gray solid) are shown. **b** ESEEM experiments performed at two fields (inset, red lines). At 2807 G, the first component (grey dotted) is predominant while at 3430 G, the second component (grey solid) is the main constituent. The spectra have been normalized to the hydrogen peak intensity (color figure online)

of coordinated histidine residues. In particular, as the number of distal nitrogen coordination increases with increase in histidine coordination, the overall intensity of the ^{14}N peak in the ESEEM spectrum will increase [51, 53, 54]. As can be seen in Fig. 4b, the ESEEM spectrum obtained at the 2807 G differ significantly from that obtained at 3430 G. Furthermore, the ESEEM spectrum at 3430 G shows a peak at 2.8 MHz. When Cu^{2+} ion is directly coordinated to the carbonyl of an amino acid residue, the amide nitrogen results in a peak at 2.8 MHz in the ESEEM spectrum [55]. Thus, the Cu^{2+} binding site corresponding to the second component possibly shows backbone coordination with the carbonyl group of the amino acid residue.

To ascertain the difference in coordination at the two binding sites and to confirm the presence of backbone coordination, we performed HYSCORE at the two fields. At 2807 G, comprising mostly of the first component, there is no observable peak at 2.8 MHz corresponding to the backbone coordination as shown in Fig. 5a. Furthermore, HYSCORE also shows no trace of backbone coordination. However, at 3430 G, ESEEM spectrum shows a sharp peak at 2.8 MHz (Fig. 5b). On analyzing HYSCORE data at 3430 G, we observe cross peaks at (4.3, 2.8 MHz). The position

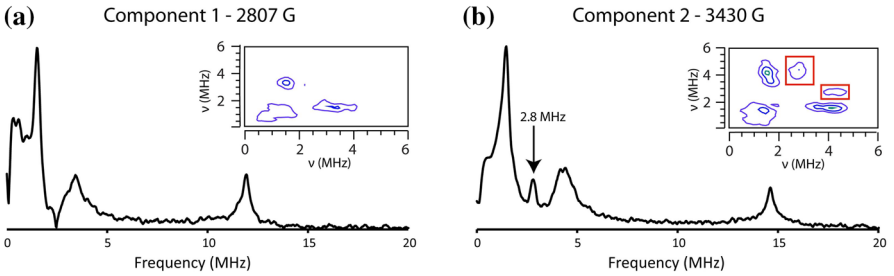

Fig. 5 **a** ESEEM spectrum at 2807 G showing no visible peak at 2.8 MHz corresponding to backbone coordination. Inset shows HYSCORE data at 2807 G which show no visible cross peaks either. **b** ESEEM spectrum at 3430 G shows a sharp peak at 2.8 MHz which could be due to possible backbone coordination. HYSCORE data (inset) show cross peaks (red squares) at (4.3, 2.8 MHz) confirming the presence of backbone coordination (color figure online)

of these cross peaks is indicative of an amide nitrogen atom of the peptide backbone when the adjacent carbonyl group is coordinated to the Cu^{2+} ion [55, 56]. Thus, only one of the Cu^{2+} binding sites is shown to undergo backbone coordination with the amino acid residue, confirming the observation that the two Cu^{2+} binding sites show different coordination environment.

Since metals have been shown to induce oligomerization of S100 proteins [20, 57–61], we further analyzed the distances between the Cu^{2+} binding sites from the X-ray crystal structure of S100A12 (PDB: 1ODB) [20] as shown in Fig. 6a. The crystal structure shows the asymmetric unit is a hexamer assembled from a trimer of dimers. The intra-dimer Cu^{2+}–Cu^{2+} distance is ~ 3 nm. There are also inter-dimer distances of ~ 1.4 nm, 4 nm and 4.8 nm contained within the hexamer.

To compare these data to that in solution, we performed Cu^{2+}–DEER [62–64] on the Ca^{2+}-loaded S100A12 with 2 equivalents of Cu^{2+}. The baseline-corrected DEER signal and the distance distribution are shown in Fig. 6b, c. First, we notice that for a pump pulse of 16 ns, the modulation depth experimentally obtained is ~ 12.6%, as

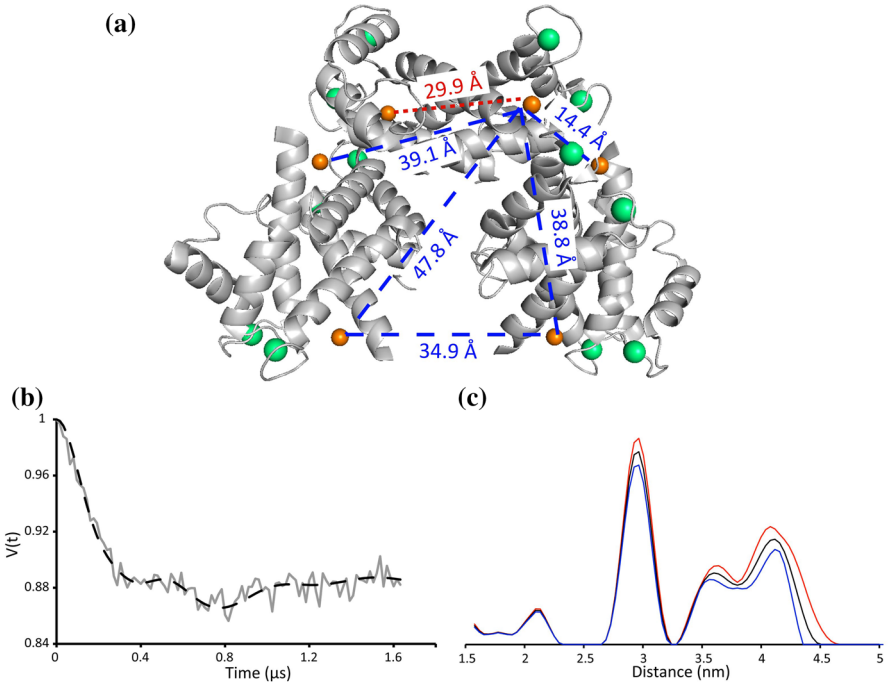

Fig. 6 **a** X-ray crystal of S100A12 bound to both Ca^{2+} and Cu^{2+} (PDB: 1ODB) [20]. The green spheres represent the Ca^{2+} ions while the orange spheres represent the Cu^{2+} ions. The blue dashed lines show the inter-dimer distances while the red dotted line shows the intra-dimer distance. **b** Background subtracted time-domain DEER data showing the presence of two frequencies. The experimental data are represented by the gray solid line and the black dashed line represents the best fit obtained from Tikhonov regularization. The modulation depth is observed to be ~ 12.6%. **c** Distance distributions obtained using Tikhonov regularization. The distribution also shows validation techniques including upper (red) and lower (blue) acceptable limits (color figure online)

shown in Fig. 6b. This is higher than the theoretical modulation depth for a system of two spins (~8.2%), calculated from the echo-detected field swept spectrum as previously described [65]. The high modulation depth confirms the presence of oligomers in our sample. Second, the distance distribution, in Fig. 6c, clearly shows a sharp peak at 3 nm and a broad peak around 4 nm. This is in good agreement with the intra-dimer distance of 3 nm and the several inter-dimer distances around 4 nm obtained from crystal structure (PDB 1ODB) [20]. We also perform a two-Gaussian fit and we find that a bimodal distance of 3 nm and 4 nm best fits our data. Note that the 1.4 nm distance is unlikely to be sampled by DEER. Using the modulation depth, a rough estimate can be made on the number of dimers and trimers of dimers in solution.

Considering our sample to be a mix of two- and six-spin systems, the modulation depth is [44, 45]:

$$\lambda = x * \lambda_2 + (1 - x) * \lambda_6, \tag{1}$$

where λ is the modulation depth and x is the mole fraction of the dimer. Also λ_N is given by [66]:

$$\lambda_N = 1 - \left(1 - p_b\right)^{N-1}, \tag{2}$$

where N is the number of spins in the system, and p_b is the fraction of spins excited by the pump pulse. For a pump pulse of 16 ns, we obtain a p_b of 0.082 [65]. As shown in the crystal structure (PDB: 1ODB), S100A12 exists as a trimer of dimers [20], which would make the sample a six-spin system. Using these equations, we estimate that roughly 83% of the protein exists as dimers in solution, under the assumption that only dimers and trimers of dimers exist.

These results are interesting because they show that oligomers exist even in the solution state. To the best of our knowledge, no previous studies have investigated the role of Cu^{2+} in oligomerization of S100A12. Previous work on Calgranulin C, in the presence of Zn^{2+}, has suggested the presence of oligomers and that oligomeric forms of S100A12 are important in the activation of the inflammation receptor RAGE [14, 20, 27, 67]. Since Cu^{2+} occupies the same binding site as Zn^{2+} and shows similar coordination geometry, we expect that the addition of Cu^{2+} will also lead to oligomerization. The agreement between the DEER distance and those measured from the X-ray structure suggests that the Cu^{2+}–Ca^{2+}–S100A12 adopts a trimer of dimer hexameric structure. Additionally, these data suggest that the Cu^{2+} binds only to the transition metal binding sites at the dimer interface and not elsewhere. This is consistent with the observation that Cu^{2+} was only observed at the canonical transition metal binding sites of S100A12, despite the fact that the crystal was grown under a large excess of Cu^{2+}.

4 Conclusion

We have shown that the two binding sites of the S100A12 bind differently to Cu^{2+}. Even though S100A12 is a homodimer and the two canonical transition metal binding sites are related by symmetry, we have shown that, in solution, the two Cu^{2+}

binding sites are distinct. The CW-ESR spectrum of Cu^{2+} bound to the protein clearly shows the presence of two components, corresponding to two different binding environments. ESEEM and HYSCORE validate these findings and show that only one of the components undergoes backbone coordination, indicating that the binding environment of the Cu^{2+} ion is different at the two sites. DEER data further confirmed that the difference in coordination is not due to Cu^{2+} binding to previously unidentified sites. The agreement of each of the most probable distance of the DEER distribution to that of the X-ray crystal structure confirms that the Cu^{2+} binds only to the canonical S100 metal binding sites located at the dimer interface. Moreover, the distances at 3 and 4 nm confirm the formation of oligomers in the presence of Cu^{2+} and Ca^{2+} and highlight the utility of ESR spectroscopy to characterize metal-induced protein oligomerization in solution.

Acknowledgements This work was supported by the National Science Foundation (awards NSF MCB-1613007 and NSF MRI-1725678 to S.S. and NSF HRD-1400969 and NSF HRD-1547757 to S.M.D.). V.G. was supported by an NSF LSAMP Bridge to the Doctorate award HRD- 1500320. We thank Dr. Matthew Lawless for useful discussion.

References

1. R. Donato, B.R. Cannon, G. Sorci, F. Riuzzi, K. Hsu, D.J. Weber, C.L. Geczy, Curr. Mol. Med. **13**, 24 (2013)
2. B.A. Gilston, E.P. Skaar, W.J. Chazin, Sci. China Life Sci. **59**, 792 (2016)
3. J.P. Zackular, W.J. Chazin, E.P. Skaar, J. Biol. Chem. **290**, 18991 (2015)
4. A.R. Bresnick, D.J. Weber, D.B. Zimmer, Nat. Rev. Cancer **15**, 96 (2015)
5. M.B. Manigrasso, J. Juranek, R. Ramasamy, A.M. Schmidt, Trends Endocrinol. Metab. **25**, 15 (2014)
6. C. Venegas, M.T. Heneka, J. Leukoc. Biol. **101**, 87 (2017)
7. D.E. Brodersen, J. Nyborg, M. Kjeldgaard, Biochemistry **38**, 1695 (1999)
8. J.A. Hayden, M.B. Brophy, L.S. Cunden, E.M. Nolan, J. Am. Chem. Soc. **135**, 775 (2013)
9. R. Glaser, J. Harder, H. Lange, J. Bartels, E. Christophers, J.M. Schroder, Nat. Immunol. **6**, 57 (2005)
10. T.E. Kehl-Fie, S. Chitayat, M.I. Hood, S. Damo, N. Restrepo, C. Garcia, K.A. Munro, W.J. Chazin, E.P. Skaar, Cell Host Microbe **10**, 158 (2011)
11. S.M. Damo, T.E. Kehl-Fie, N. Sugitani, M.E. Holt, S. Rathi, W.J. Murphy, Y. Zhang, C. Betz, L. Hench, G. Fritz, E.P. Skaar, W.J. Chazin, Proc. Natl. Acad. Sci. USA. **110**, 3841 (2013)
12. K.P. Haley, A.G. Delgado, M.B. Piazuelo, B.L. Mortensen, P. Correa, S.M. Damo, W.J. Chazin, E.P. Skaar, J.A. Gaddy, Infect. Immun. **83**, 2944 (2015)
13. J.M. Shank, B.R. Kelley, J.W. Jackson, J.L. Tweedie, D. Franklin, S.M. Damo, J.A. Gaddy, C.N. Murphy, J.G. Johnson, Infect. Immun. **86**(6), e00234-18 (2018)
14. O.V. Moroz, E.V. Blagova, A.J. Wilkinson, K.S. Wilson, I.B. Bronstein, J. Mol. Biol. **391**, 536 (2009)
15. R. Wolf, O.M. Howard, H.F. Dong, C. Voscopoulos, K. Boeshans, J. Winston, R. Divi, M. Gunsior, P. Goldsmith, B. Ahvazi, T. Chavakis, J.J. Oppenheim, S.H. Yuspa, J. Immunol. **181**, 1499 (2008)
16. M. Solioz, H.K. Abicht, M. Mermod, S. Mancini, J. Biol. Inorg. Chem. **15**, 3 (2010)
17. C. White, J. Lee, T. Kambe, K. Fritsche, M.J. Petris, J. Biol. Chem. **284**, 33949 (2009)
18. K.W. Becker, E.P. Skaar, FEMS Microbiol. Rev. **38**, 1235 (2014)
19. A.N. Besold, B.A. Gilston, J.N. Radin, C. Ramsoomair, E.M. Culbertson, C.X. Li, B.P. Cormack, W.J. Chazin, T.E. Kehl-Fie, V.C. Culotta, Infect. Immun. **86**(2), e00779-17 (2018)
20. O.V. Moroz, A.A. Antson, S.J. Grist, N.J. Maitland, G.G. Dodson, K.S. Wilson, E. Lukanidin, I.B. Bronstein, Acta Crystallogr. D Biol. Crystallogr. **59**, 859 (2003)

21. T. Nishikawa, I.S. Lee, N. Shiraishi, T. Ishikawa, Y. Ohta, M. Nishikimi, J. Biol. Chem. **272**, 23037 (1997)
22. B.W. Schafer, J.M. Fritschy, P. Murmann, H. Troxler, I. Durussel, C.W. Heizmann, J.A. Cox, J. Biol. Chem. **275**, 30623 (2000)
23. V. Sivaraja, T.K. Kumar, D. Rajalingam, I. Graziani, I. Prudovsky, C. Yu, Biophys. J. **91**, 1832 (2006)
24. L.C. Wheeler, M.J. Harms, BMC Biophys **10**, 8 (2017)
25. O.V. Moroz, A.A. Antson, E.J. Dodson, H.J. Burrell, S.J. Grist, R.M. Lloyd, N.J. Maitland, G.G. Dodson, K.S. Wilson, E. Lukanidin, I.B. Bronstein, Acta Crystallogr. D Biol. Crystallogr. **58**, 407 (2002)
26. O.V. Moroz, A.A. Antson, G.N. Murshudov, N.J. Maitland, G.G. Dodson, K.S. Wilson, I. Skibshoj, E.M. Lukanidin, I.B. Bronstein, Acta Crystallogr. D Biol. Crystallogr. **57**, 20 (2001)
27. O.V. Moroz, W. Burkitt, H. Wittkowski, W. He, A. Ianoul, V. Novitskaya, J. Xie, O. Polyakova, I.K. Lednev, A. Shekhtman, P.J. Derrick, P. Bjoerk, D. Foell, I.B. Bronstein, BMC Biochem. **10**, 11 (2009)
28. J. Xie, D.S. Burz, W. He, I.B. Bronstein, I. Lednev, A. Shekhtman, J. Biol. Chem. **282**, 4218 (2007)
29. E. Jackson, S. Little, D.S. Franklin, J.A. Gaddy, S.M. Damo, J. Vis. Exp. **123**, e55557 (2017)
30. C.D. Syme, R.C. Nadal, S.E.J. Rigby, J.H. Viles, J. Biol. Chem. **279**, 18169 (2004)
31. S. Stoll, A. Schweiger, J. Magn. Reson. **178**, 42 (2006)
32. J.M. Fauth, A. Schweiger, L. Braunschweiler, J. Forrer, R.R. Ernst, J. Magn. Reson. **66**, 74 (1986)
33. C. Gemperle, G. Aebli, A. Schweiger, R.R. Ernst, J. Magn. Reson. **88**, 241 (1990)
34. M. Pannier, S. Veit, A. Godt, G. Jeschke, H.W. Spiess, J. Magn. Reson. **142**, 331 (2000)
35. G. Jeschke, V. Chechik, P. Ionita, A. Godt, H. Zimmermann, J. Banham, C.R. Timmel, D. Hilger, H. Jung, Appl. Magn. Reson. **30**, 473 (2006)
36. A.M. Bowen, M.W. Jones, J.E. Lovett, T.G. Gaule, M.J. McPherson, J.R. Dilworth, C.R. Timmel, J.R. Harmer, Phys. Chem. Chem. Phys. **18**, 5981 (2016)
37. A.J. Fielding, S. Fox, G.L. Millhauser, M. Chattopadhyay, P.M.H. Kroneck, G. Fritz, G.R. Eaton, S.S. Eaton, J. Magn. Reson. **179**, 92 (2006)
38. T. Ostendorp, J. Diez, C.W. Heizmann, G. Fritz, Biochim. Biophys. Acta **1813**, 1083 (2011)
39. J.I. Murray, M.L. Tonkin, A.L. Whiting, F. Peng, B. Farnell, J.T. Cullen, F. Hof, M.J. Boulanger, BMC Struct. Biol. **12**, 16 (2012)
40. H. Lin, G.R. Andersen, L. Yatime, BMC Struct. Biol. **16**, 8 (2016)
41. B. Shin, S. Saxena, Biochemistry **47**, 9117 (2008)
42. R. Aasa, T. Vanngard, J. Magn. Reson. **19**, 308 (1975)
43. S. Ruthstein, K.M. Stone, T.F. Cunningham, M. Ji, M. Cascio, S. Saxena, Biophys. J. **99**, 2497 (2010)
44. M.J. Lawless, S. Ghosh, T.F. Cunningham, A. Shimshi, S. Saxena, Phys. Chem. Chem. Phys. **19**, 20959 (2017)
45. S. Ghosh, M.J. Lawless, G.S. Rule, S. Saxena, J. Magn. Reson. **286**, 163 (2018)
46. I.M. Klotz, J. Biol. Chem. **279**, 1 (2004)
47. I.M. Klotz, Arch. Biochem. **9**, 109 (1946)
48. R. Gesztelyi, J. Zsuga, A. Kemeny-Beke, B. Varga, B. Juhasz, A. Tosaki, Arch. Hist. Exact Sci. **66**, 427 (2012)
49. M.I. Stefan, N. Le Novère, PLoS Comput. Biol. **9**, e1003106 (2013)
50. D.L. Nelson, M.M. Cox, A.L. Lehninger, *Lehninger Principles of Biochemistry* (W.H. Freeman and Company, New York, 2013)
51. K.I. Silva, B.C. Michael, S.J. Geib, S. Saxena, J. Phys. Chem. B **118**, 8935 (2014)
52. B.K. Shin, S. Saxena, J. Phys. Chem. A **115**, 9590 (2011)
53. J. McCracken, P.R. Desai, N.J. Papadopoulos, J.J. Villafranca, J. Peisach, Biochemistry **27**, 4133 (1988)
54. D. Goldfarb, J.-M. Fauth, Y. Tor, A. Shanzer, J. Am. Chem. Soc. **113**, 1941 (1991)
55. C.S. Burns, E. Aronoff-Spencer, C.M. Dunham, P. Lario, N.I. Avdievich, W.E. Antholine, M.M. Olmstead, A. Vrielink, G.J. Gerfen, J. Peisach, W.G. Scott, G.L. Millhauser, Biochemistry **41**, 3991 (2002)
56. P. Dorlet, S. Gambarelli, P. Faller, C. Hureau, Angew. Chemie **121**, 9437 (2009)
57. M.B. Brophy, J.A. Hayden, E.M. Nolan, J. Am. Chem. Soc. **134**, 18089 (2012)
58. L.S. Cunden, A. Gaillard, E.M. Nolan, Chem. Sci. **7**, 1338 (2016)
59. I.P. Korndorfer, F. Brueckner, A. Skerra, J. Mol. Biol. **370**, 887 (2007)

60. N. Leukert, T. Vogl, K. Strupat, R. Reichelt, C. Sorg, J. Roth, J. Mol. Biol. **359**, 961 (2006)
61. T. Ostendorp, E. Leclerc, A. Galichet, M. Koch, N. Demling, B. Weigle, C.W. Heizmann, P.M. Kroneck, G. Fritz, EMBO J. **26**, 3868 (2007)
62. Z. Yang, D. Kise, S. Saxena, J. Phys. Chem. B **114**, 6165 (2010)
63. Z. Yang, M.R. Kurpiewski, M. Ji, J.E. Townsend, P. Mehta, L. Jen-Jacobson, S. Saxena, Proc. Natl. Acad. Sci. USA. **109**, E993 (2012)
64. M. Ji, S. Ruthstein, S. Saxena, Acc. Chem. Res. **688**, 688 (2014)
65. Z. Yang, M. Ji, S. Saxena, Appl. Magn. Reson. **39**, 487 (2010)
66. A.D. Milov, Y.D. Tsvetkov, F. Formaggio, M. Crisma, C. Toniolo, J. Raap, J. Am. Chem. Soc. **112**, 3843 (2000)
67. K.-W. Hung, C.-C. Hsu, C. Yu, J. Biomol. NMR **57**, 313 (2013)

Affiliations

Shreya Ghosh[1] · Velia Garcia[2,3] · Kevin Singewald[1] · Steven M. Damo[2,3] · Sunil Saxena[1]

✉ Steven M. Damo
sdamo@fisk.edu

✉ Sunil Saxena
sksaxena@pitt.edu

[1] Department of Chemistry, University of Pittsburgh, Pittsburgh, PA 15260, USA

[2] Department of Chemistry, Fisk University, Nashville, TN 32708, USA

[3] Department of Biochemistry and Center for Structural Biology, Vanderbilt University, Nashville, TN 37232, USA